Quantitative imaging of the optical near field

Paul Kühler,[1,2,4,5] **F. Javier García de Abajo,**[3] **Philipp Leiprecht,**[1,2]
Andreas Kolloch,[1] **Javier Solis,**[2] **Paul Leiderer,**[1] **and Jan Siegel**[2,*]

[1]*Faculty of Physics, Universität Konstanz, Universitätsstraße 10, 78457 Konstanz, Germany*
[2]*Instituto de Optica, CSIC, Serrano 121, 28006 Madrid, Spain*
[3]*Instituto de Química Física "Rocasolano," CSIC, Serrano 119, 28006 Madrid, Spain*
[4]*Current affiliation: Faculty of Physics, Ludwig-Maximilians-Universität München,*
Amalienstraße 54, 80799 München, Germany
[5]*paul.kuehler@lmu.de*

[*]*j.siegel@io.cfmac.csic.es*

Abstract: When exposing small particles on a substrate to a light plane wave, the scattered optical near field is spatially modulated and highly complex. We show, for the particular case of dielectric microspheres, that it is possible to image these optical near-field distributions in a quantitative way. By placing a single microsphere on a thin film of the photosensitive phase change material $Ge_2Sb_5Te_5$ and exposing it to a single short laser pulse, the spatial intensity modulation of the near field is imprinted into the film as a pattern of different material phases. The resulting patterns are investigated by using optical as well as high-resolution scanning electron microscopy. Quantitative information on the local optical near field at each location is obtained by calibrating the material response to pulsed laser irradiation. We discuss the influence of polarization and angle of incidence of the laser beam as well as particle size on the field distribution. The experimental results are in good quantitative agreement with a model based on a rigorous solution of Maxwell's equations. Our results have potential application to near-field optical lithography and experimental determination of near fields in complex nanostructures.

© 2012 Optical Society of America

References and links

1. M. Ohtsu, *Optical Near Fields: Introduction to Classical and Quantum Theories of Electromagnetic Phenomena at the Nanoscale* (Springer, 2004).
2. A. Plech, V. Kotaidis, M. Lorenc, and J. Boneberg, "Femtosecond laser near-field ablation from gold nanoparticles," Nat. Phys. **2**, 44–47 (2005).
3. Y. Tanaka, G. Obara, A. Zenidaka, M. Terakawa, and M. Obara, "Femtosecond laser near-field nano-ablation patterning using Mie resonance high dielectric constant particle with small size parameter," Appl. Phys. Lett. **96**, 261103 (2010).
4. E. McLeod and C. B. Arnold, "Subwavelength direct-write nanopatterning using optically trapped microspheres," Nat. Nanotechnol. **3**, 413–417 (2008).
5. H. J. Lezec, "Beaming light from a subwavelength aperture," Science **297**, 820–822 (2002).
6. A. Kramer, W. Trabesinger, B. Hecht, and U. P. Wild, "Optical near-field enhancement at a metal tip probed by a single fluorophore," Appl. Phys. Lett. **80**, 1652–1654 (2002).
7. Z. Wang, W. Guo, L. Li, B. Luk'yanchuk, A. Khan, Z. Liu, Z. Chen, and M. Hong, "Optical virtual imaging at 50 nm lateral resolution with a white-light nanoscope," Nat. Commun. **2**, 218 (2011).

8. D. Brodoceanu, L. Landström, and D. Bäuerle, "Laser-induced nanopatterning of silicon with colloidal monolayers," Appl. Phys. A. **86**, 313–314 (2007).

9. R. Morarescu, L. Englert, B. Kolaric, P. Damman, R. A. L. Vallee, T. Baumert, F. Hubenthal, and F. Träger, "Tuning nanopatterns on fused silica substrates: a theoretical and experimental approach," J. Mater. Chem. **21**, 4076–4081, (2011).

10. Z. B. Wang, M. H. Hong, B. S. Luk'yanchuk, Y. Lin, Q. F. Wang, and T. C. Chong, "Angle effect in laser nanopatterning with particle-mask," J. Appl. Phys. **96**, 6845–6850 (2004).

11. A. Pereira, D. Grojo, M. Chaker, P. Delaporte, D. Guay, and M. Sentis, "Laser-fabricated porous alumina membranes for the preparation of metal nanodot arrays," Small **4**, 572–576 (2008).

12. P. Leiderer, C. Bartels, J. König-Birk, M. Mosbacher, and J. Boneberg, "Imaging optical near-fields of nanostructures," Appl. Phys. Lett. **85**, 5370–5372 (2004).

13. P. Kühler, F. J. García de Abajo, J. Solis, M. Mosbacher, P. Leiderer, C. Afonso, and J. Siegel, "Imprinting the optical near field of microstructures with nanometer resolution," Small **5**, 1825–1829 (2009).

14. J. Siegel, D. Puerto, J. Solis, F. J. García de Abajo, C. N. Afonso, M. Longo, C. Wiemer, M. Fanciulli, P. Kühler, M. Mosbacher, and P. Leiderer, "Ultraviolet optical near-fields of microspheres imprinted in phase change films," Appl. Phys. Lett. **96**, 193108 (2010).

15. M. Wuttig, and N. Yamada, "Phase-change materials for rewriteable data storage," Nat. Mater. **6**, 824–832 (2007).

16. R. Ovshinsky, "Reversible electrical switching phenomena in disordered structures," Phys. Rev. Lett. **21**, 1450–1453 (1968).

17. V. Weidenhof, I. Friedrich, S. Ziegler, and M. Wuttig, "Laser induced crystallization of amorphous $Ge_2Sb_5Te_5$ films," J. Appl. Phys. **89**, 3168–3176 (2001).

18. Y. Lin, M. H. Hong, T. C. Chong, C. S. Lim, G. X. Chen, L. S. Tan, Z. B. Wang, and L. P. Shi, "Ultrafast-laser-induced parallel phase-change nanolithography," Appl. Phys. Lett. **89**, 041108 (2006).

19. B. Lee, J. Abelson, S. Bishop, D. Kang, B. Cheong, and K. Kim, "Investigation of the optical and electronic properties of $Ge_2Sb_5Te_5$ phase change material in its amorphous, cubic, and hexagonal phases," J. Appl. Phys. **97**, 1–8 (2005).

20. F. J. García de Abajo, G. Gómez-Santos, L. A. Blanco, A. G. Borisov, and S. V. Shabanov, "Tunneling mechanism of light transmission through metallic films," Phys. Rev. Lett. **95**, 067403 (2005).

21. G. Mie, "Beiträge zur Optik trüber Medien, speziell kolloidaler Metallösungen," Ann. d. Phys. **330**, 377–445 (1908).

22. J. M. Liu, "Simple technique for measurements of pulsed gaussian-beam spot sizes," Opt. Lett. **7**, 196–198 (1982).

23. B. S. Luk'Yanchuk, Z. B. Wang, W. D. Song, M. H. Hong, "Particle on surface: 3D-effects in dry laser cleaning," Appl. Phys. A-Mater. **79**, 747–751 (2004).

24. J. Siegel, W. Gawelda, D. Puerto, C. Dorronsoro, J. Solis, C. N. Afonso, J. C. G. de Sande, R. Bez, A. Pirovano, and C. Wiemer, "Amorphization dynamics of $Ge_2Sb_5Te_5$ films upon nano- and femtosecond laser pulse irradiation," J. Appl. Phys. **103**, 023516 (2008).

25. H. Ishikawa, H. Tamaru, and K. Miyano, "Microsphere resonators strongly coupled to a plane dielectric substrate: coupling via the optical near field," J. Opt. Soc. Am. A, Vol. **17**, 802-813 (2000).

26. T. Sannomiya, and C. Hafner, "Multiple multipole program modelling for nano plasmonic sensors," J. Comput. Theor. Nanoscience **7**, 1587–1595 (2010).

27. N. Stefanou, V. Yannopapas, and A. Modinos, "Heterostructures of photonic crystals: frequency bands and transmission coefficients," Comput. Phys. Commun. **113**, 49-77 (1998).

28. F. J. García de Abajo, A. Rivacoba, N. Zabala, and P. M. Echenique, "Electron energy loss spectroscopy as a probe of two-dimensional photonic crystals," Phys. Rev. B **68**, 205105 (2003).

29. F. J. García de Abajo, "Multiple scattering of radiation in clusters of dielectrics," Phys. Rev. B **60**, 6086–6102 (1999).

---

1. Introduction

The ultimate performance of key technologies in photonics is limited by the diffraction of light, which can be overcome by using optical near fields (ONFs) [1]. ONFs can be generated, for instance, in the vicinity of metal nanoparticles [2], dielectric spheres [3, 4], subwavelength apertures [5], or at the tip of an atomic force microscope [6].

In the particular case of dielectric spheres, local intensity distributions can be achieved with super-resolution foci, which can be exploited in a white-light optical microscope to achieve 50 nm lateral resolution [7]. Parallel nanostructuring employing colloidal monolayers of dielectric microspheres has been successfully demonstrated to pattern silicon [8], fused silica [9], as well as GeSbTe [10] and alumina films [11].

In order to use ONFs for applications in a predictable and controlled way with maximum precision, it is essential to have a detailed knowledge of the exact field distribution. A straightforward method to study local optical field distributions of micro- and nanostructures is to imprint them onto the underlying substrate. This method bears many advantages over classical near-field characterization methods such as scanning near-field optical microscopy (SNOM). For example, the system is not disturbed by the scanning microscope tip and the actual imprinting of the optical field distribution is done during a very short time (i.e., with a single laser pulse) in contrast to typically time-consuming scanning processes. This minimizes possible sample degradation effects.

A well-known example of the imprinting technique is the visualization of near fields by local ablation of the substrate, in which regions exposed to large field enhancements are ablated, leaving behind a crater whose morphology is related to the shape of the field distribution [12]. A major disadvantage of this method is its binary contrast (i.e., ablation/no ablation) and the presence of non-linear and collateral effects (e.g., debris). Recently, a different method has been demonstrated [13, 14], which relies on local phase change from crystalline to amorphous in thin chalcogenide films [15]. Laser-induced amorphization requires melting and rapid quenching in order to prevent nucleation and growth of the crystalline phase. The required high cooling rates of the molten film can be achieved by using a short (nanosecond) laser pulse and a substrate with high thermal conductivity to act as a heat sink. Here, the imprinted field distribution yields a non-binary optical contrast over a large range of illumination intensity and is not affected by collateral or non-linear effects. Yet, while previous work has reported a general qualitative agreement in pattern shape between experiment and calculation, a quantitative agreement in field enhancement could not be provided.

In the present work, we demonstrate that it is possible to image ONFs not only in terms of shape but also quantitatively in terms of local field enhancement. The experimental results, imprinting ONFs of dielectric spheres and their variation as a function of particle diameter and light polarization, are in excellent agreement with a model based on solving Maxwell's equations for a sphere sitting on a layered planar substrate. We also show that high-resolution SEM studies of imprinted patterns yield well-contrasted ONF images and reveal fine structures not resolvable with optical microscopy.

Although in this work we focus on the optical and morphological contrast between the two GST phases, it is worth mentioning that a phase change is also accompanied by a change in the electrical resistivity [16], topography [17], and etching resistivity, the latter allowing for parallel production of features with an FWHM below 50 nm [18].

This paper is organized as follows. In Section 2, experimental details and a description of the model and quantitative analysis method are given. In Section 3, the optical response of GST to laser pulses of different durations (fs, ps, and ns) is examined in detail, which serves the purpose of calibration. The results are then integrated into the calculation to relate the optical response of ONFs to the corresponding field enhancement by comparison with the model. We compare the patterns produced by spheres of different sizes exposed to laser radiation of different incident polarization, illustrating the strong connection between particle size, polarization, and near field distribution. In Section 4, we correlate the optical contrast of the patterns used so far to the contrast obtained from scanning electron microscopy (SEM) measurements [14].

2. Experimental and modeling

2.1. Sample preparation

The samples consisted of 40-nm-thick, face-centered-cubic (fcc) polycrystalline $Ge_2Sb_5Te_5$ (GST) films sputter-deposited on Si [001] wafers which is covered by a 10-nm-thick amorphous SiO_2 buffer layer, produced by Numonyx, Italy. The optical constants of the different

materials at the laser wavelength used in the experiment (800 nm) are for fcc-GST: $n = 5.72$, $k = 4.09$ [19]; amorphous GST: $n = 4.74$, $k = 1.45$ [19]; amorphous SiO_2: $n = 1.453$, $k = 0$; Si: $n = 3.69$, $k = 0.006$. Spherical SiO_2 glass particles, dispersed in isopropanol, were deposited under conditions that ensure particle isolation. The particles used have nominal diameters of 660 nm, 4.83 μm (Bangs Laboratories, Inc., nominal polydispersity 2%), and 990 nm (Duke Scientific Corp., polydispersity $< 10\%$). The size distribution was checked after deposition with a scanning electron microscope (SEM). It revealed small deviations from the nominal sizes (573 ± 44 nm, 1003 ± 16 nm, and 4645 ± 27 nm, respectively). These values have been used as input parameters for the calculations presented later on.
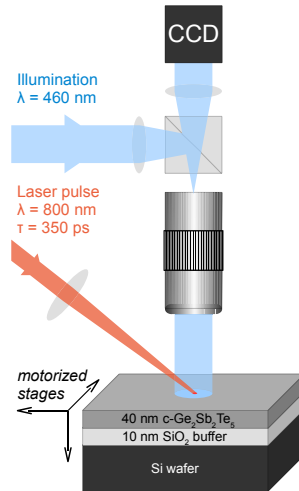

Fig. 1. Setup used for irradiation with single laser pulses, including a home-built in-situ microscope and a movable stage holding the sample. The configuration of the layered substrate is also shown.

2.2. Sample irradiation

Laser irradiation of the particle covered films was performed in air using a regeneratively amplified Ti:sapphire laser system operating at 800 nm central wavelength with a pulse duration of 120 fs, 350 ps, or 8 ns. The different pulse durations were achieved by compressing the chirped pulse after amplification (fs), not compressing it (ps), or blocking the fs-laser oscillator seed pulse and operating the amplifier in a Q-switched mode (ns). A sketch of the irradiation scheme is displayed in Fig. 1. The laser beam was focused onto the sample at an angle of incidence of $\sim 53°$ to a measured elliptical spot size of $270 \times 150 \,\mu m^2$ ($1/e^2$ diameter). A single pulse was selected from a 100 Hz pulse train by means of an electromechanical shutter to irradiate the targeted area. The sample was mounted on a motorized translation stage (three axis) and observed in-situ with a home-built microscope based on a long working distance microscope objective (20x, numerical aperture $NA = 0.42$) and a tube lens, equipped with a 12 bit charge-coupled device (CCD) camera and illuminated by a light emitting diode (LED) (wavelength $\lambda = 400$ nm).

2.3. Characterization of the imprinted microstructures

Bright-field images of the irradiated regions were recorded *ex-situ* with a commercial microscope (Eclipse, Nikon) using an illumination wavelength of 460 nm and a high-magnification objective lens (100x, $NA = 0.90$). Additionally, SEM high-resolution studies were performed

with the in-lens detector of a Zeiss Gemini Supra at an accelerating voltage in the range of 5 kV, yielding a nominal spatial resolution of 5 nm.

2.4. Modeling of the intensity distribution

The spatial electric field distribution at the substrate plane has been calculated by a rigorous solution of Maxwell's equations for a sphere sitting on a layered planar substrate, using methods similar to those proposed in Ref. [20], and fully elaborated in the appendix. The incident-light plane wave has a well-defined linear polarization and is incident on the substrate at an angle of 53°. The resulting field is expanded into spherical waves around the sphere, and Mie scattering theory [21] is used to determine the resulting outgoing waves. The latter are expressed as plane waves (both propagating and evanescent) moving towards the substrate, and reflected from the surface using Fresnel's coefficients. The reflected plane waves are in turn scattered by the sphere, so that a self-consistent set of equations is written to describe the infinite series of alternating multiple scattering events at the sphere and the substrate. The system is further reduced by integrating over parallel wave vector components of the plane-wave part of the field, leading to a set of linear equations involving only spherical-wave coefficients, which we solve for all multipoles up to an orbital angular number $l = 24$ for full convergence. Finally, the electric field intensity is calculated right underneath the surface, thus giving the fraction of light that penetrates into the film and is absorbed. The latter assumption is justified by the short penetration length of 16 nm for light with a wavelength of 800 nm (i.e., no significant interference is expected as the light propagates within the substrate, so that the dependence of the near-field intensity on the distance to the surface is assumed to be a simple exponential dictated by the skin depth and shared by all points of the surface). Full details of the calculation method are given in the appendix.

3. Optical studies

In this chapter, we concentrate on the optical contrast generated upon laser-induced phase change for analyzing the field distributions imprinted in the GST films. In particular, we show that a quantitative determination can be achieved. Once the optical response is characterized, this can be applied to the study of different size particles for different polarization of the incident light.

3.1. Optical response of GST to laser irradiation

Figure 2(a) shows an optical micrograph of the surface reflectivity of a GST film after irradiation with a 350 ps pulse. The modified region is elliptically elongated due to the inclined incidence. The beam has a Gaussian profile, which was characterized by measuring the diameter of the amorphous region in the irradiated area at different pulse energies. Therefore, the exact spatial fluence distribution on the substrate surface of the incident beam can be precisely determined [22].

In the inset, both the reflectivity and the corresponding fluence distribution are plotted along the dashed line in the micrograph. Far away from the spot center, the film is in an unmodified, crystalline state characterized by a reflectivity R_0. With increasing fluence, the normalized reflectivity R/R_0 first drops to a minimum value of 0.73, then recovers slightly, and finally ends in a step, which marks the edge of the central ablation crater, where the GST film is completely removed from the substrate. From direct comparison of the irradiation fluence with the reflectivity of the film after irradiation at a certain position, one can obtain a response function of the GST film for a given set of irradiation parameters (Fig. 2(b)).

For ps pulses, the modification starts at 23 mJ/cm^2 and the minimum reflectivity R is reached at 56 mJ/cm^2. Between these two values, the reflectivity is a monotonously decreasing function
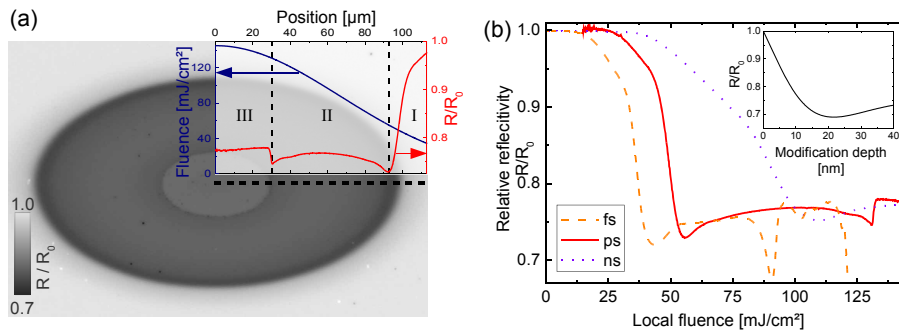
Fig. 2. Optical response of a crystalline GST film to irradiation with single laser pulses of different durations. (a) Micrograph of the film exposed to irradiation at oblique incidence ($\tau = 350\,ps$, $\theta = 53°$ off normal), producing an amorphous ring (regions I and II) around the spot center, where ablation of the GST has taken place (region III). Superimposed is the fluence distribution of the Gaussian beam at the sample surface and the relative reflectivity change of the film along the dashed line. (b) Relative reflectivity change of the sample as a function of the local fluence for different pulse durations. The inset shows the reflectivity change as a function of the thickness of the amorphized top layer of the GST film based on a model assuming interfacial amorphization.

of laser fluence. Keeping the pulse wavelength fixed at 800 nm, we have investigated the influence of pulse duration τ on the response of the film. For all three values of τ, the minimum reflectivity is reached at a fluence value three times higher than the onset of amorphization. This implies that in a first approximation the optical response curve can simply be scaled for different τ's. With increasing τ, the heat flow during the pulse duration of the deposited laser energy towards the substrate increases, thus efficiently reducing the maximum peak temperature. As a consequence, a higher fluence is required to compensate the heat loss and reach the onset of amorphization for increasing τ, so that the whole response function is stretched over a larger fluence interval [24]. While these results demonstrate that an equivalent optical response curve can be obtained for all three (and other intermediate) pulse durations, we concentrate in the following on results obtained with 350 ps pulses.

The behavior of the GST film in the amorphous-response regime can be qualitatively explained by assuming an interfacial transformation of the crystalline GST layer into an amorphous one, starting from its surface and with the thickness of the transformed layer being a monotonous function of the irradiated fluence [24]. The inset of Fig. 2(b) shows the calculated reflectivity of the system as a function of the thickness of the amorphized GST layer. The model gives good qualitative agreement as it well reproduces the recovery below the ablation threshold.

With these results, any complex pattern with different reflectivity values can be mapped directly into the correspondent fluence distribution that created the pattern. Even if this fluence window is exceeded, by inverting this analysis a calculated fluence distribution can be converted into the expected resulting reflectivity pattern, as shown in the next section.

3.2. *Near-field patterns of dielectric spheres: Quantitative analysis*

While the relation established above between optical contrast and local fluence is satisfactory but not too exciting for irradiation of the bare surface with a Gaussian spot, it enables us to

analyze and quantify complex spatial field distributions, which form upon irradiation of scattering particles. The micrograph depicted in Fig. 3(a) shows the result of such an irradiation for a 350 ps pulse on a SiO$_2$ particle with a diameter of $1.00\,\mu$m, which was removed upon irradiation. Its position can be determined from the ablation hole that is left behind at the focal position of the particle and is indicated by a white dot. Due to the oblique incidence ($\theta = 53°$, from the left), the imprinted pattern, composed of amorphous and crystalline regions, is elliptically elongated and only symmetrical with respect to the horizontal axis through the particle center. In the intermediate vicinity of the particle, the pattern is complex, in contrast to the far field of the scattering particle where the period p of the observed fringes along the surface-projected forward and backward light propagation directions equals a constant value ($p_{fw,exp} = 3.9\,\mu$m and $p_{bw,exp} = 440$ nm, respectively). A simple calculation of the interference of a spherical wave for the scattered light with the incident plane wave yields $p_{fw} = \lambda_{inc}/(1 - \sin\theta) = 3.97\,\mu$m along the forward direction and $p_{bw} = \lambda_{inc}/(1 + \sin\theta) = 445$ nm along the backward direction, both in good agreement with the measured value.
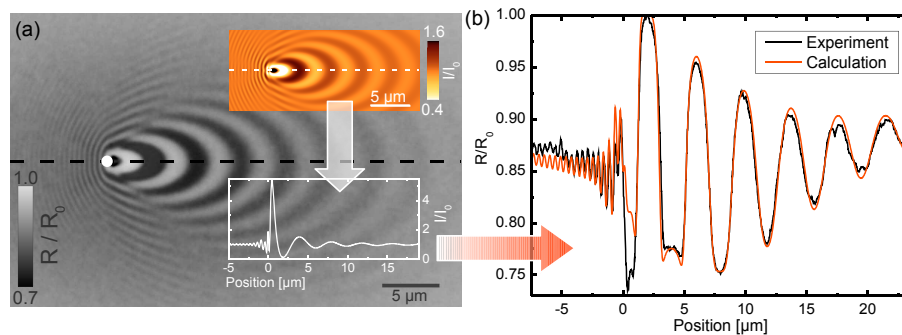

Fig. 3. Quantitative comparison between the optical near-field imprint produced by irradiation of a single dielectric sphere on the GST film and the corresponding calculation. (a) Optical micrograph of the GST film after irradiation with a 350 ps pulse ($\theta = 53°$) on a sphere (diameter $d = 1.00\,\mu$m), which was removed upon irradiation. The particle's original position is marked with a white dot. Also shown is the corresponding calculated intensity distribution as well as the intensity profile along the white dashed line (both as insets). (b) Reflectivity profiles along the horizontal axis through the center of the sphere. The experimental data were taken along the black dashed line in (a). Calculated data are obtained from mapping the theoretical intensity profile shown in the inset of (a) into reflectivity values (see main text for details).

For a deeper understanding of the field distribution in the particle near field, it is necessary to compare the resulting pattern with a calculation that takes into account the whole system and therefore also includes the influence of the substrate. The need for such a comparison becomes obvious if one looks at the close vicinity of the particle, where the far-field condition is not met. The shadowing effect of the particle cannot explain the considerable spatial extension of the apparently unmodified, bright region around the ablation hole that is much larger than the particle projection onto the surface. Using the model described in section 2, the two-dimensional intensity distribution $I/I_0(x, y)$ for the present arrangement was calculated and is depicted as an inset in Fig. 3(a). For a qualitative, spatial comparison with experiment, these values are shown with an inverted color scale (i.e. dark regions mark field enhancement whereas brighter regions mark field attenuation). In this way the calculations reflect the GST behavior as an approximate opposite linear function of the local fluence upon irradiation.

Since $I/I_0(x,y) \propto F/F_0(x,y)$, the value of I_0 can be directly determined from the measured pulse peak fluence $F_{max} = 18.6 \, \text{mJ/cm}^2$ at the beam center position. Finally, the profile was convoluted with a Gaussian function which simulates the limitation in spatial resolution imposed by the imaging system. The result, displayed in Fig. 3(b), shows an excellent agreement between calculation and experiment. Deviations are in the range of only a few percent, except for the range $0 < x < 1 \, \mu\text{m}$, where the particle focuses the incoming light down to a very small area, leading to strong local ablation in this region.

3.3. Influence of the particle size on the imprinted pattern

To investigate the influence of particle size on the field distribution, we irradiated colloidal spheres of different diameters (Fig. 4). The laser beam was polarized perpendicular to the incident plane (s-polarized). In all cases, the particles have been removed upon irradiation.
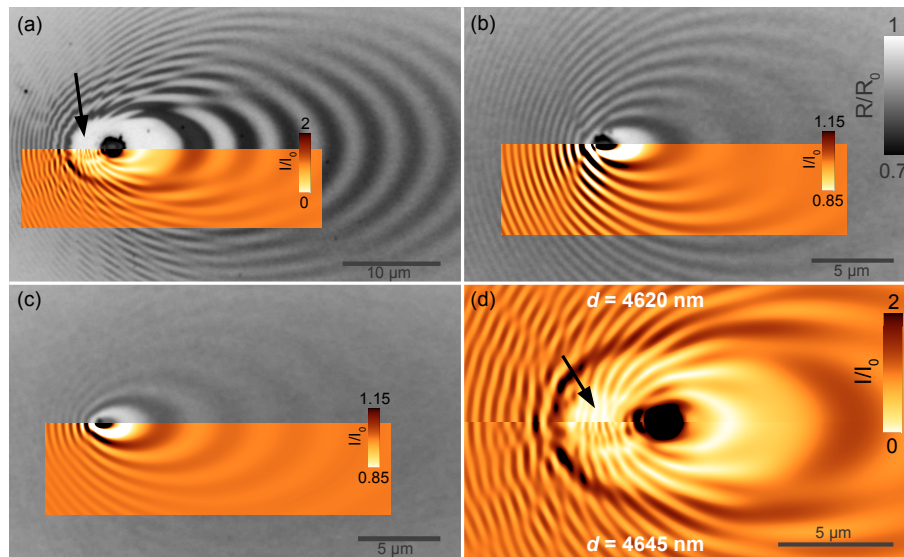

Fig. 4. Near-field imprints from particles of different sizes. (a) Optical micrograph of the GST film after irradiation with a 350 ps pulse ($\theta = 53°$) on a single sphere (d = 4.65 μm). The calculated intensity distribution is shown as an inset. (b) Same as (a) for $d = 1.00 \, \mu\text{m}$. (c) Same as (a) for $d = 0.57 \, \mu\text{m}$. (d) Lower part: Calculated intensity distribution from (a). Upper part: Calculated intensity distribution for a particle diameter that is only 25 nm smaller than in (a).

With increasing particle size, two trends become apparent: Firstly, the near-field pattern is more complex for larger particles. The smallest particles investigated, with a diameter comparable to the wavelength of the incident light, display a characteristic pattern similar to that of a simple dipole (Fig. 4(c)). In contrast, the situation is more complex for bigger particles (Fig. 4(a)). This applies only to the near-field of the particles (i.e. up to distances that are comparable to the diameter of the scattering particle). For all investigated particle sizes, at distances $x \geq 2d$ from the particle center, the diameter-independent far-field behavior of the modulation periods quoted above ($p_{fw/bw} = \lambda_{inc}/(1 \pm \sin\theta)$) holds quite satisfactorily. The second effect, which also concerns the far-field of the particles, is that the amplitude of the interference pattern decreases with the particle size, in agreement with the smaller scattering cross section.

As in the previous figure, the agreement between imprints and calculated intensity distributions is very good. However, for the largest particle there are some differences in the "shadow region" to the left of the ablation hole (c.f. arrow in Fig. 4(a)). In particular, the calculation predicts a field enhancement fine structure in contrast to the experimental pattern, where the film is found to remain in its original crystalline phase at this position. In order to estimate the effect of small deviations in the particle size used for the calculation, the field distribution for a particle with a diameter only 25 nm smaller (i.e. within the margin of error of the measurement) was calculated and compared to the one shown in Fig. 4(a). Both results cannot be distinguished when examining only the forward-scattering part, but they feature significant differences in the shadow region. The subtle modulation in the field distribution at this position vanishes completely for the smallest particle (black arrow), which fits well to the experimentally resulting pattern. Those subtle field enhancements in the shadow region of the particle are in agreement with calculation results of previous work by Luk'Yanchuk et al. [23].
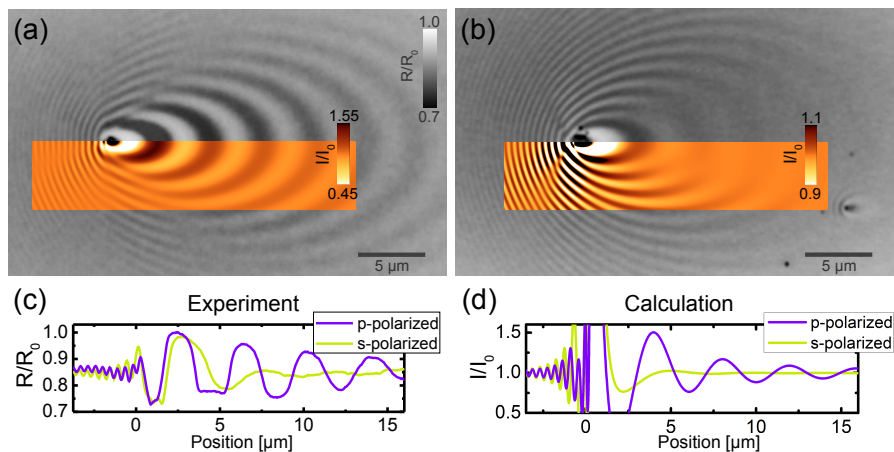

Fig. 5. Near-field imprints of particles with diameter $d = 1.00\,\mu$m for different linear polarizations of the 350 ps laser pulse. (a) Micrograph of a pattern produced with p-polarized light. The calculated intensity distribution is shown as an inset. (b) Same as (a) for s-polarized light. (c) Reflectivity profile along a line in the incident plane and through the particle center (at $x = 0$) in (a) and (b). (d) Corresponding calculated intensity profiles.

The polarization of the incident light also has a great influence on the imprinted pattern. Figure 5 shows two patterns that are the result of irradiations on particles of the same size ($d = 1.00\,\mu$m) but for different beam polarizations. Besides the obvious differences in the shape of both imprints, more subtle features can be distinguished when plotting the horizontal reflectivity profiles through the particle center for both polarizations (Fig. 5(c)). The forward-scattering part of the pattern produced by p-polarized light is much more pronounced than for s-polarized light. The opposite behavior is observed for the back-scattering and side parts, which accordingly are visible over a much larger area in Fig. 5(b). Both observations are in agreement with the corresponding calculation, which predicts this exact relative local field amplification (Fig. 5(d)).

4. SEM studies

The optical studies reported in section 3 demonstrate the ability of our method to image optical near-fields in a quantitative manner. Yet, a higher spatial resolution, as provided by SEM, is desirable as it can resolve even the smallest features within the imprinted patterns. In order

to use SEM for this purpose, the SEM contrast produced by laser-induced modification of a crystalline GST film needs to be characterized as a first step.

4.1. Characterization of SEM contrast in laser irradiated GST film

Figure 6 shows a comparison of a SEM micrograph with an optical-microscope image, both taken at the same spot. The pulse energy was much higher than that used in Fig. 2. Thus, the ablation crater is larger and includes a second ring, which marks the onset of ablation of the SiO_2 buffer layer underneath. Interestingly, at this magnification it is difficult to distinguish the amorphous region from the surrounding crystalline film with SEM. Only the regions at irradiation fluences well within the amorphization regime show up in SEM, slightly darker than the neighboring surface to the right. In order to understand the origin of the different SEM contrast in the amorphous part of the spot, a series of regions along the horizontal axis through the beam center position were investigated at higher resolution. Due to carbon deposition during the SEM scans, these regions appear darker in the overview shown in Fig. 6.

At the position that is furthest away from the irradiated area (position 7(a) in Fig. 6), the high resolution SEM scan reveals the characteristic roughness of the unmodified, polycrystalline GST film (Fig. 7(a)). In the intermediate amorphous region, which shows little difference with respect to the crystalline surface observed with SEM at low magnification, ripples of larger period show up at high magnification (Fig. 7(b)). Finally, at the position nearest to the ablation threshold (full amorphization), the surface becomes smooth (Fig. 7(b)).
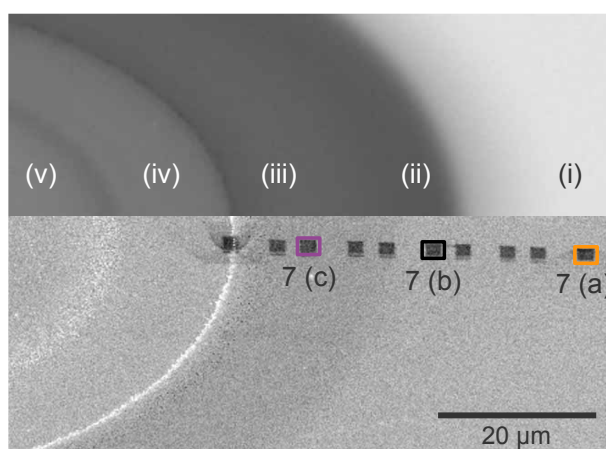

Fig. 6. Upper part: Optical micrograph of a zoomed region of an irradiated area without particles ($\tau = 350$ ps). From right to left, the intensity increases and gives rise to different optical response of the sample: (i) crystalline GST film, (ii) partially amorphized GST film, (iii) completely amorphized GST film (iv) ablation of GST film, and (v) ablation of buffer layer. Lower part: SEM micrograph of the same irradiated spot. The darkened rectangular regions were investigated at higher resolution (see Fig. 7).

In order to analyze the surface morphology in more detail, the images were processed with fast Fourier transform (FFT). An example of the result of FFT is displayed for Fig. 7(b) as an inset. Subsequently, the isotropic distributions were radially averaged for noise reduction. The resulting contour plots were then normalized to their mean values at high frequencies, where the signal distribution is nearly homogeneous. The signal artifacts introduced by FFT due to limited dimensions of the processed images were eliminated in the data obtained from Fig. 7(a) and (b) by subtracting the result of Fig. 7(c), since no characteristic frequency band was found.
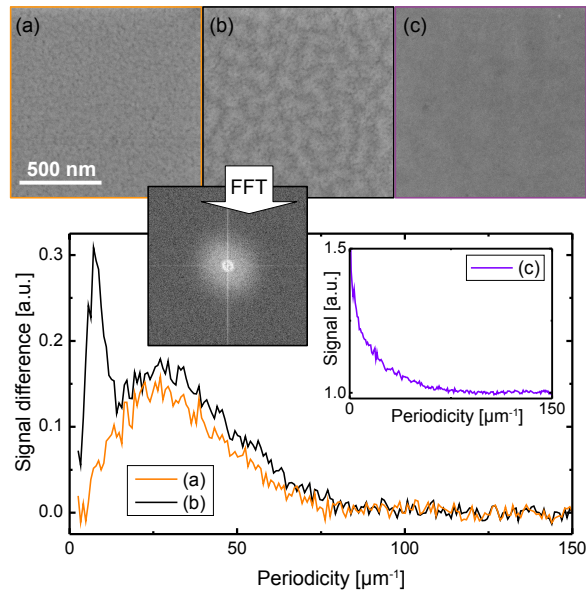
Fig. 7. (a)-(c) SEM micrographs of the GST film in different states (marked in Fig. 6). (a) crystalline GST, (b) partially amorphized GST, and (c) completely amorphized GST. The Fourier transforms of all images (example shown for (b)), radially integrated and normalized, are plotted in the graphs below. The result from (c) mainly consists of background noise (see graph inset: signal vs. periodicity), which is common to all transforms and which was therefore subtracted from the results of (a) and (b), displaying signal difference versus periodicity in the plot.

The final result reveals that the ripples in the partly amorphous region do not replace, but rather superimpose, the roughness that is inherited by the crystalline film. Namely, the only difference between (a) and (b) is the formation of a sharp peak at a period of $\sim 130\,$nm, which adds to the less pronounced peak at a period of $\sim 40\,$nm. This is the grain size of the as-grown crystalline GST film. Both structural components vanish at larger fluence (c), leaving behind a smooth, fully amorphous GST film.

In summary, we find that depending on the local fluence the GST film yields a ternary SEM contrast: Crystalline with a grain size of 40 nm (I), partially amorphized with superimposed ripples of a period three times larger than the crystalline film grain size (II), and completely amorphous and smooth (III). Identification of this behavior enables us to carry out an advanced interpretation of complex near field patterns imprinted when irradiating the GST film with a particle on top of it.

4.2. SEM investigation of near field patterns

High-resolution images are especially interesting in the region of the pattern back-scattering, where the period of the produced structure is very small and cannot be resolved completely with optical microscopy. An illustrative SEM micrograph of a pattern produced by a particle with $d = 4645\,$nm is shown in Fig. 8(a) along with the corresponding calculation. The pattern contains features corresponding to all three regimes identified above. Most fringes are composed of ripples (regime II), the space between fringes and the shadow region is unmodified (regime I) and the first fringe, close to the shadow region, is smooth and dark (regime III). The ripple

period coincides with the one observed in the type-II contrast regime, as discussed before.

The level of detail that can be accessed using SEM becomes clear when examining the "shadow region" of the irradiated particle. The region around the ablation hole is not completely unmodified, as one could erroneously deduce from the optical-microscope results. Instead, the fine tips of the imprinted interference maxima almost reach the ablation hole (white arrow). These subtle structures are also predicted by the calculation.
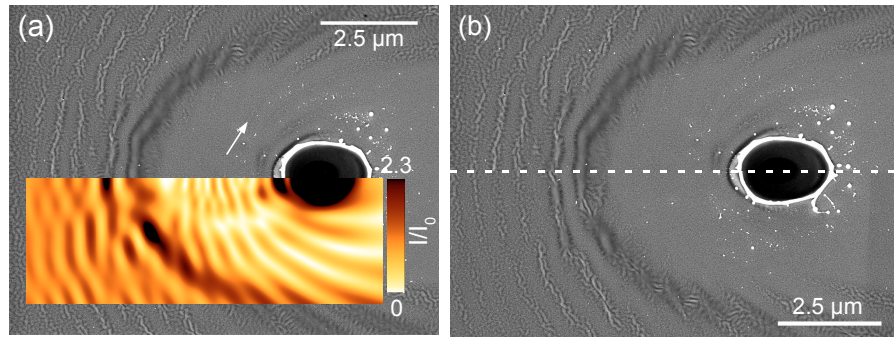

Fig. 8. SEM-micrographs of the near-field pattern of a particle (diameter $d = 4645\,\text{nm}$) at the position where it was located before irradiation ($\tau = 350\,\text{ps}$). The corresponding calculated intensity distribution is shown as an inset in (a). (b) Upper part: taken from the SEM micrograph shown in (a). Lower part: taken from a SEM micrograph of a pattern of a particle with the same size but exposed to lower pulse energy.

In Fig. 8(b), the SEM image of (a) is contrasted with another irradiation at lower pulse energy (lower half of the picture). The lower amount of deposited energy leads to less pronounced features in the imprint. Regarding the inner-most fringes located in the vicinity of the "shadow", not only the width but also the contrast type is different. In the upper part of the figure, these fringes are mainly of type-III contrast (smooth and dark borders), whereas in the lower part, at the corresponding location, only a type-II contrast (with ripples) is found. A comparison with theory in Fig. 8(a) confirms that the type III-contrast regions are formed at positions of high intensity. This leads to the conclusion that the fluence-dependent surface morphology that is observed upon laser irradiation of the bare GST film is also maintained at a much smaller scale. Accordingly, the altered regions in the particle pattern correspond to the calculated field enhancements not only in terms of shape, but also quantitatively in a sense of the ternary contrast of the bare GST surface as discussed above. Finally, it appears that the smallest feature size that is possible to be produced with this technique is not yet reached as the surface roughness is still smaller than the imprinted pattern period.

5. Conclusions

We have demonstrated that the imprinting of optical near-fields originating from single colloidal particles in GST films enables the imaging of complex field distributions in full detail and even quantitative analysis of the so-produced features. The particle size and the polarization of the incoming light are found to have a strong influence on the form and modulation depth of the imprints. The results are quantitatively matched with calculations based on rigorous solution of the Maxwell's equations with only small deviations within a few percent. Optical contrast allows for the visualization of a high dynamic range of field distributions, whereas

SEM imaging shows that the GST film yields a ternary contrast in the crystalline-amorphous regime. High-resolution SEM images show the capability of GST films to record the fine structure of optical near-fields in great detail, in excellent agreement with theoretical calculations. Further down-scaling of optically written patterns in GST films seems to be possible and we are currently identifying suitable structures to produce such small scattering field distributions. Our technique is inherently applicable to other types of scattering particles, such as plasmonic colloids.

6. Appendix

In this appendix we provide a semi-analytical method to solve Maxwell's equations for the geometry of the samples examined in this paper. Alternative methods to describe equivalent situations have been reported previously [23, 25]. We consider a spherical particle placed close to a substrate, as shown in Fig. 9, illuminated by a light plane wave coming from region I. We solve the electromagnetic field in this configuration by expanding it in terms of plane and spherical waves in the three regions shown in the Fig. and then matching them at their boundaries. Similar methods have been used for other configurations, and they are generally known as multiple multipolar expansions [26]. We work in frequency space, so that the notation $\mathbf{E}(\mathbf{r},t) = \mathbf{E}(\mathbf{r})\exp(-i\omega t) + \text{c.c.}$ is used for the fields. The origin $\mathbf{r} = 0$ is chosen at the substrate point that is closest to the sphere.

In the numerical calculations shown in this paper, we introduce Fresnel's coefficients to represent the layered substrate used in the experiment. The resulting reflection coefficients can be expressed in terms of the Fresnel coefficients of each interface, as explained in Ref. [27].
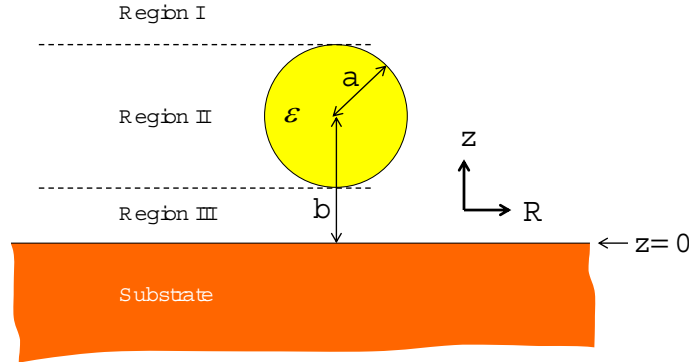

Fig. 9. Elements used in the description of the response of a homogeneous spherical particle of radius a sitting near a substrate. We eventually set $b = a$ in the calculations reported in this paper.

The incident plane wave has wave vector components $\mathbf{Q}_0$ along the x and y directions parallel to the substrate and $-q_0 = -\sqrt{k^2 - Q_0^2 + i0^+}$ along z, where k is the light wave vector in the air medium above the substrate and the sign of the square root is chosen to yield $\text{Im}\{q_0\} > 0$. Given the symmetry of the sphere-substrate system, it is convenient to expand the incident electric field, taken to have unit amplitude, in terms of cylindrical waves as

$$\mathbf{E}_0(\mathbf{r}) = \begin{cases} \hat{\mathbf{e}}_p e^{i\mathbf{Q}_0\cdot\mathbf{R} - iq_0 z} = -\sum_m i^m \mathbf{E}_{Q_0 mp}^-, & \text{for } \sigma_0 = p \text{ polarization}, \\ \hat{\mathbf{e}}_s e^{i\mathbf{Q}_0\cdot\mathbf{R} - iq_0 z} = \sum_m i^{m+1} \mathbf{E}_{Q_0 ms}^-, & \text{for } \sigma_0 = s \text{ polarization}, \end{cases} \tag{1}$$

where $\hat{\mathbf{e}}_p$ and $\hat{\mathbf{e}}_s$ are the polar and azimuthal unit vectors, respectively, and

$$\mathbf{E}_{Qms}^{\pm} = \left[\frac{im}{QR} J_m(QR)\hat{\mathbf{R}} - J_m'(QR)\hat{\varphi} \right] e^{im\varphi} e^{\pm iqz},$$

$$\mathbf{E}_{Qmp}^{\pm} = \pm \frac{q}{k} \left[iJ_m'(QR)\hat{\mathbf{R}} - \frac{m}{QR} J_m(QR)\hat{\varphi} \pm \frac{Q}{q} J_m(QR)\hat{\mathbf{z}} \right] e^{im\varphi} e^{\pm iqz}$$

form a complete basis set of cylindrical waves (see the appendix of Ref. [28] for further details on these types of waves). Here, R and φ are the polar coordinates of $\mathbf{R} = (x, y)$, the origin of z is at the substrate plane, and $q = \sqrt{k^2 - Q^2 + i0^+}$. We can solve the problem separately for each azimuthal component m and then sum the results with the same coefficients as in the expansion of Eq. (1).

We thus need to find the self-consistent electromagnetic field for each incident cylindrical wave $\mathbf{E}_{Q_0 m \sigma_0}^-$ of parallel wave vector Q_0, polarization σ_0, and azimuthal number m. The electric field in region I becomes

$$\mathbf{E} = \mathbf{E}_{Q_0 m \sigma_0}^- + \sum_\sigma \int_0^\infty QdQ \, \beta_{Q\sigma} \, \mathbf{E}_{Qm\sigma}^+, \qquad (2)$$

where $r_{Q\sigma}$ is the Fresnel reflection coefficient of the layered substrate for polarization σ and parallel wave vector Q, and the second term on the right hand side comes from the scattering produced by the sphere and the substrate, expressed in terms of cylindrical waves with expansion coefficients $\beta_{Q\sigma}$. Likewise, the field in region III can be written

$$\mathbf{E} = \sum_\sigma \int_0^\infty QdQ \, \gamma_{Q\sigma} \left[\mathbf{E}_{Qm\sigma}^- + r_{Q\sigma}\mathbf{E}_{Qm\sigma}^+ \right]. \qquad (3)$$

Finally, the field in region II contains the waves impinging into it (i.e., the incident wave and the waves reflected at the substrate) plus the spherical waves scattered out of the sphere:

$$\mathbf{E} = \mathbf{E}_{Q_0 m \sigma_0}^- + \sum_\sigma \int_0^\infty QdQ \, \gamma_{Q\sigma} \, r_{Q\sigma}\mathbf{E}_{Qm\sigma}^+ + \sum_{l\sigma} \alpha_{l\sigma}\mathbf{E}_{lm\nu}^h,$$

where

$$\mathbf{E}_{lmM}^h = \mathbf{L} h_{lm}^{(+)}(\mathbf{r} - \mathbf{r}_0),$$

$$\mathbf{E}_{lmE}^h = (-i/k)\nabla \times \mathbf{L} h_{lm}^{(+)}(\mathbf{r} - \mathbf{r}_0)$$

are spherical outgoing waves of magnetic (M) and electric (E) polarization, $\mathbf{L} = -i(\mathbf{r} - \mathbf{r}_0) \times \nabla$ is the orbital angular momentum operator relative to the center of the sphere $\mathbf{r}_0$, and $h_{lm}^{(+)}(\mathbf{r}) = i^l h_l^{(+)}(kr) Y_{lm}(\hat{\mathbf{r}})$ is an outgoing scalar spherical wave (see Ref. [29] for more details on spherical waves).

Obviously, we need to transform the electric field back and forth between spherical and cylindrical waves. The spherical outgoing waves produced by scattering at the sphere can be written in terms of cylindrical waves as

$$\mathbf{E}_{lm\nu}^h = \sum_\sigma \int_0^\infty QdQ M_{Q\sigma,l\nu}^{\pm} \mathbf{E}_{Qm\sigma}^{\pm},$$

where the $+$ ($-$) sign stands for waves propagation above (below) the sphere, away from it. Likewise, the cylindrical waves incident on the sphere can be expanded in spherical waves as

$$\mathbf{E}_{Qm\sigma}^{\pm} = \sum_{l=|m|}^{\infty} \sum_\nu N_{l\nu,Q\sigma}^{\pm} \mathbf{E}_{lm\nu}^j,$$

where $\mathbf{E}^j_{lmv}$ is the same as $\mathbf{E}^h_{lmv}$ with the spherical Hankel function $h^{(+)}_l$ substituted by the spherical Bessel function j_l. Following the methods described in Refs. [27, 29], we find the following analytical expressions for the expansion coefficients in these equations:

$$M^{\pm}_{Qp,lM} = -iM^{\pm}_{Qs,lE}$$
$$= \mp e^{\pm iqd}\frac{i^{m+1}}{qk}\left[\frac{\pm q}{k}\left(\sqrt{(l+m+1)(l-m)}\,Y_{l,m+1} + \sqrt{(l-m+1)(l+m)}\,Y_{l,m-1}\right) - \frac{2mQ}{k}Y_{l,-m}\right],$$

$$M^{\pm}_{Qs,lM} = -iM^{\pm}_{Qp,lE} = \pm e^{\pm iqd}\frac{i^{m+1}}{qk}\left(\sqrt{(l+m+1)(l-m)}\,Y_{l,m+1} - \sqrt{(l-m+1)(l+m)}\,Y_{l,m-1}\right)$$

and

$$N^{\pm}_{Q\sigma,lv} = \frac{2\pi i(-1)^{m+1}(\pm qk)}{l(l+1)}\,e^{\mp 2iqd}\,M^{\pm}_{Q\sigma,lv},$$

where the spherical harmonics are evaluated as $Y_{lm} = (-1)^m\sqrt{(2l+1)(l-m)!/4\pi(l+m)!}\,P_{lm}(\pm q/k)$ for $m \le 0$ in terms of Legendre polynomials P_{lm}, and $Y_{lm} = (-1)^m Y_{l,-m}$ for $m < 0$.

We also need the Mie scattering coefficients of the sphere t_{lv} (independent of m), so that each spherical wave $\mathbf{E}^j_{lmv}$ incident on the sphere produces a scattered wave $t_{lv}\mathbf{E}^h_{lmv}$. These coefficients take the explicit form [29]

$$t_{lM} = \frac{-j_l(\rho_0)\rho_1 j'_l(\rho_1) + \rho_0 j'_l(\rho_0)j_l(\rho_1)}{h^{(+)}_l(\rho_0)\rho_1 j'_l(\rho_1) - \rho_0[h^{(+)}_l(\rho_0)]' j_l(\rho_1)},$$

$$t_{lE} = \frac{-j_l(\rho_0)[\rho_1 j_l(\rho_1)]' + \varepsilon[\rho_0 j_l(\rho_0)]' j_l(\rho_1)}{h^{(+)}_l(\rho_0)[\rho_1 j_l(\rho_1)]' - \varepsilon[\rho_0 h^{(+)}_l(\rho_0)]' j_l(\rho_1)},$$

where $\rho_0 = ka$, $\rho_1 = ka\sqrt{\varepsilon + i0^+}$ with $\mathrm{Im}\{\rho_1\} > 0$, a is the sphere radius, ε is its dielectric function, and the prime denotes differentiation with respect to ρ_0 and ρ_1.

We can directly write the following self-consistent relation for the coefficients $\gamma_{Q\sigma}$:

$$\gamma_{Q\sigma} = \delta_{\sigma\sigma_0}\frac{\delta(Q-Q_0)}{Q} + \sum_{lv}M^-_{Q\sigma,lv}t_{lv}N^-_{lv,Q_0\sigma_0} + \sum_{lv}M^-_{Q\sigma,lv}t_{lv}\sum_{\sigma'}\int_0^\infty Q'dQ' N^+_{lv,Q'\sigma'}r_{Q'\sigma'}\gamma_{Q'\sigma'},$$

where the first term in the right-hand side represents the incident wave, the second term comes from the scattering of the incident wave at the sphere, and the third term describes the reflection at the substrate and the scattering by the sphere. We solve this equation upon discretization of the integral using a finite set of points Q_n as

$$\int_0^\infty dQ' F(Q') \approx \sum_n F(Q_n)\Delta Q_n.$$

In practice, convergence is achieved with ~ 400 points. Additionally, well converged results are obtained by limiting the sums over spherical waves to $l < 20-30$. The problem of finding the expansion coefficients is thus reduced to linear algebra, which in matrix notation becomes $\gamma = (1 - M^- \cdot t \cdot N^+ \cdot r)^{-1} \cdot [(1 + M^- \cdot t \cdot N^-) \cdot E_0]$, where the dots denote matrix multiplication and the components of E_0 are readily obtained from Eq. (1). This yields the expansion coefficients γ, out of which we obtain the field right outside the substrate plane by means of Eq. (3). The field intensity acting on the material is obtained from the continuity of the parallel electric-field components and the perpendicular electric displacement. Incidentally, the far-field is given by Eq. (2), with the coefficients β obtained from $\beta = r \cdot \gamma + M^+ \cdot t \cdot (N^- \cdot E_0 + N^+ \cdot r \cdot \gamma)$.

Acknowledgments